A Non-ordinary State-based Godunov-peridynamics Formulation for Strong Shocks in Solids

Guohua Zhou* Michael Hillman†

March 7, 2019

Abstract

The theory and meshfree implementation of peridynamics has been proposed to model problems involving transient strong discontinuities such as dynamic fracture and fragment-impact problems. For effective application of numerical methods to these events, essential shock physics and Gibbs instability should be addressed. The Godunov scheme for shock treatment has been shown an effective approach for tackling these two issues but has not been considered yet for peridynamics. This work introduces a physics-based shock modeling formulation for non-ordinary state-based peridynamics, in which the Godunov scheme is introduced by embedding the Riemann solution into the force state, resulting in a shock formulation free of tuneable parameters. Several benchmark problems are solved to demonstrate the effectiveness of the proposed formulation for modeling problems involving shocks in solids.

Keywords: peridynamics, meshfree, shockwaves, Godunov scheme

1 Introduction

The theory of peridynamics [1, 2] has been proposed to effectively model problems that involve dynamic strong discontinuities such as dynamic fracture and fragment-impact problems. It bypasses essential difficulties of classic continuum mechanics in fracture modeling due to the invalidity of taking spatial derivatives across cracks and necessity for geometric descriptions of arbitrary three-dimensional propagating crack surfaces, by directly working on an integral form of governing equations that does not involve any spatial derivatives.

The first peridynamics model is called bond-based peridynamics [1] which was proposed to model the formation of discontinuities in elastic brittle solids. As a nonlocal theory, bonds are defined between a point and all of its neighboring points within a zone called a horizon. The two points in a single bond interact via a spring-like force depending on only the stretch of the bond itself, and cracks can be naturally modeled by the breakage of the bonds. This method has been applied to dynamic crack branching in brittle glass [3, 4], impact and damage of layered glass [5] and damage in concrete [6], among other problems.

However, the bond-based peridynamics formulation suffers from restrictions on the material response, for example, Poisson's ratio is limited to a fixed value. Meanwhile, constitutive laws need to be developed specifically for peridynamics. To overcome these limitations, state-based peridynamics [2] was introduced. In this formulation, the bond force depends on the collective deformation of all the bonds within a horizon rather than a single bond independently, as in the bond-based model. The so-called non-ordinary state-based peridynamics based on correspondence [2] defines the constitutive response through a non-local deformation gradient, and can thus incorporate classical constitutive

*Research Scientist, Optimal Inc., Plymouth, MI 48170

†Kimball Assistant Professor, The Pennsylvania State University, University Park, PA 16802; corresponding author, mhillman@psu.edu

models. It has been applied to ballistic impact of aluminum panels [7], high velocity impact [8], and dynamic fracture of aluminum [9].

Although the non-ordinary state-based peridynamics has been widely applied to model high strain rate problems, there is limited work published on shock modeling. Shock wave propagation is an important physics to be considered in numerical methods for problems such as high-velocity impact and blast, where peridynamics has great advantage due to its natural ability to model transient discontinuities. In [10, 11], the artificial viscosity technique was employed to treat shocks in peridynamics. This approach is simple to implement, but involves tunable parameters, which is undesirable since it can lead to parameter-dependent results that are not objective. In [12] artificial dissipation via a rate-dependent material model was introduced for the same purpose, with similar limitations.

An effective approach for shock modeling is the class of Godunov schemes originating from the method proposed by Godunov [13] under the finite difference framework. In these methods, the jump conditions and the entropy solution are embedded by solving a Riemann problem defined at cell interfaces. They have been extended to the discontinuous Galerkin method [14], smoothed particle hydrodynamics [15], the finite point method [16], among other methods [17–22]. Higher order Godunov schemes [23, 24] have also been developed to enhance accuracy. Under the reproducing kernel particle method framework [25, 26] with stabilized conforming nodal integration (SCNI) [27], a Riemann-SCNI method [28, 29] has been developed to introduce the Godunov scheme by a Riemann solution enriched pressure gradient, smoothed over SCNI cells.

In this paper, the Godunov scheme is embedded into the non-ordinary state-based peridynamics, and the resulting formulation is termed Godunov-peridynamics. First, the force state is expressed in terms of Cauchy stress, and separated into volumetric and deviatoric contributions since the pressure dominates the Cauchy stress under strong shocks. Effective surface information between two points is then obtained by drawing an analogy between the resulting discrete peridynamic formulation and the finite volume method. This surface information is then used to define a Riemann problem between two points, and the Riemann solution is then employed in the volumetric force state to embed shock physics into state-based peridynamics.

The remainder of this paper is organized as follows. In Section 2, the non-ordinary state-based peridynamics formulation is reviewed. In Section 3, the Godunov-peridynamics formulation is then introduced. Numerical implementation of the proposed method is given in Section 4. Numerical results are then presented in Section 5 to demonstrate the effectiveness of the proposed method, followed by discussions and conclusions in Section 6.

2 Non-ordinary state-based peridynamics formulation

In this section, we briefly review the non-ordinary state-based peridynamics formulation [2]. Let $\mathbf{x}$ and $\mathbf{X}$ denote coordinates in the deformed and undeformed configuration respectively. A continuum point $\mathbf{X}$ interacts non-locally with its neighbors within a horizon H with measure δ as shown in Figure 1. The bond of a point $\mathbf{X}_I$ with another point $\mathbf{X}_J$ in the undeformed configuration is

$$\mathbf{X}_{I:J} = \mathbf{X}_J - \mathbf{X}_I. \tag{1}$$

The same bond in the deformed configuration is denoted as

$$\mathbf{x}_{I:J} = \mathbf{x}_J - \mathbf{x}_I. \tag{2}$$

A nonlocal deformation gradient $\mathbf{F}_I$ at point I can be computed via the principle of constitutive correspondence [2] as

$$\mathbf{F}_I = \Big(\int_{\mathrm{H}_{\mathbf{X}_I}} \omega_{I:J} \mathbf{x}_{I:J} \otimes \mathbf{X}_{I:J} dV_{\mathbf{X}_J} \Big) \cdot \mathbf{K}_I^{-1}, \tag{3}$$

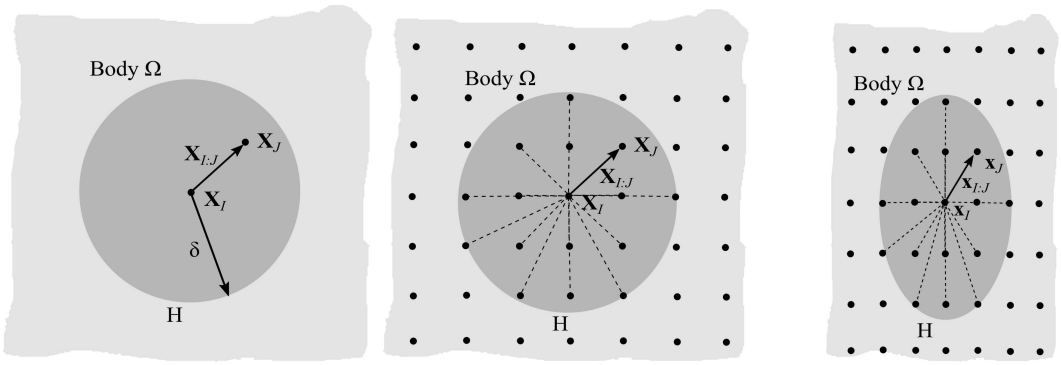

(a) undeformed continuum (b) undeformed discretized (c) deformed discretized

Figure 1: Schematic of peridynamics representations: continuum and discrete cases.

where $\mathbf{K}_I$ is the shape tensor defined as

$$\mathbf{K}_I = \int_{\mathrm{H}_{\mathbf{X}_I}} \omega_{I:J} \mathbf{X}_{I:J} \otimes \mathbf{X}_{I:J} dV_{\mathbf{X}_J}, \tag{4}$$

and $\omega_{I:J}$ is the so-called influence function which is a function of the distance between point I and J. In this paper, the Lagrangian peridynamics formulation is adopted; the influence function is defined in terms of material distance, and $\mathrm{H}_{\mathbf{X}_I}$ and $dV_{\mathbf{X}_J}$ in the above equations are the horizon of point I and volume associated with point J respectively, in the undeformed configuration.

For the influence function, the following cubic spline function is chosen:

$$\omega_{I:J}\langle \mathbf{X}_{I:J} \rangle = \begin{cases} \dfrac{2}{3} - 4\left|\dfrac{\mathbf{X}_{I:J}}{\delta}\right|^2 + 4\left|\dfrac{\mathbf{X}_{I:J}}{\delta}\right|^3 & \text{for } 0 \le \left|\dfrac{\mathbf{X}_{I:J}}{\delta}\right| \le \dfrac{1}{2}, \\ \dfrac{4}{3} - 4\left|\dfrac{\mathbf{X}_{I:J}}{\delta}\right| + 4\left|\dfrac{\mathbf{X}_{I:J}}{\delta}\right|^2 - \dfrac{4}{3}\left|\dfrac{\mathbf{X}_{I:J}}{\delta}\right| & \text{for } \dfrac{1}{2} \le \left|\dfrac{\mathbf{X}_{I:J}}{\delta}\right| \le 1, \\ 0 & \text{otherwise,} \end{cases} \tag{5}$$

where δ is the radius of the horizon $\mathrm{H}_{\mathbf{X}_I}$ as shown in Figure 1 (a). The above influence function smoothly vanishes at the horizon boundary, which helps to improve the accuracy of numerical integration [30].

The force state between point I and J in terms of the first Piola-Kirchhoff stress tensor $\boldsymbol{\sigma}$ under correspondence is computed from the state $\underline{\mathbf{T}}_{I:J}$ acting on a bond $\mathbf{X}_{I:J}$:

$$\underline{\mathbf{T}}_{I:J}\langle \mathbf{X}_{I:J} \rangle = \omega_{I:J} \boldsymbol{\sigma}_I(\mathbf{F}_I) \cdot \mathbf{K}_I^{-1} \cdot \mathbf{X}_{I:J} \tag{6}$$

where $\boldsymbol{\sigma}_I(\mathbf{F}_I)$ is given by the constitutive model. The angle bracket in the above is used to denote the variable that a state operates on. The final equation of motion in the non-ordinary state-based peridynamics formulation at a point I is

$$\rho_I \ddot{\mathbf{u}}_I - \int_{\mathrm{H}_{\mathbf{X}_I}} \left(\underline{\mathbf{T}}_{I:J}\langle \mathbf{X}_{I:J} \rangle - \underline{\mathbf{T}}_{J:I}\langle \mathbf{X}_{J:I} \rangle \right) dV_{\mathbf{X}_J} - \mathbf{b}_I = 0 \tag{7}$$

where ρ_I is the density, $\ddot{\mathbf{u}}_I$ is the acceleration ($\mathbf{u}_I$ is the displacement), and $\mathbf{b}_I$ is the external body force density, at point I.

3 Godunov-peridynamics formulation

In the presence of shock waves, equation (7) with the force state given by (6) leads to severely oscillating nonphysical solutions due to lack of consideration of shock physics and Gibbs instability. To address these issues, the Godunov scheme [13] is introduced into the peridynamics formulation, which is discussed in this section.

3.1 Equation of motion

For convenience, the integrand of the second term in (7) is first expressed as

$$\underline{\hat{\mathbf{T}}}_{I:J} = \underline{\mathbf{T}}_{I:J}\langle \mathbf{X}_{I:J}\rangle - \underline{\mathbf{T}}_{J:I}\langle \mathbf{X}_{J:I}\rangle \tag{8}$$

where $\underline{\hat{\mathbf{T}}}_{I:J}$ is the total force state between point I and J. Substitution of (6) into (8) yields the expression in terms of the first Piola-Kirchhoff stress

$$\underline{\hat{\mathbf{T}}}_{I:J} = \omega_{I:J}\boldsymbol{\sigma}_I(\mathbf{F}_I)\cdot\mathbf{K}_I^{-1}\cdot\mathbf{X}_{I:J} - \omega_{J:I}\boldsymbol{\sigma}_J(\mathbf{F}_J)\cdot\mathbf{K}_J^{-1}\cdot\mathbf{X}_{J:I}. \tag{9}$$

Making use of the fact that $\omega_{I:J} = \omega_{J:I}$ and $\mathbf{X}_{I:J} = -\mathbf{X}_{I:J}$, equation (9) can be rewritten as

$$\underline{\hat{\mathbf{T}}}_{I:J} = \omega_{I:J}\big(\boldsymbol{\sigma}_I(\mathbf{F}_I)\cdot\mathbf{K}_I^{-1} + \boldsymbol{\sigma}_J(\mathbf{F}_J)\cdot\mathbf{K}_J^{-1}\big)\cdot\mathbf{X}_{I:J}. \tag{10}$$

Employing the relationship between Cauchy stress $\boldsymbol{\tau}$ and the first Piola-Kirchhoff stress

$$\boldsymbol{\sigma} = \boldsymbol{\tau}\cdot\mathbf{F}^{-T}\det(\mathbf{F}) \tag{11}$$

where $\det(\mathbf{F})$ is the determinant of the nonlocal deformation gradient $\mathbf{F}$, equation (10) can be expressed as

$$\underline{\hat{\mathbf{T}}}_{I:J} = \omega_{I:J}\big(\boldsymbol{\tau}_I\cdot\mathbf{F}_I^{-T}\cdot\mathbf{K}_I^{-1}\det(\mathbf{F}_I) + \boldsymbol{\tau}_J\cdot{\mathbf{F}_J}^{-T}\cdot\mathbf{K}_J^{-1}\det(\mathbf{F}_J)\big)\cdot\mathbf{X}_{I:J}. \tag{12}$$

Since the pressure is the dominant portion of the Cauchy stress in strong shock problems, the stress tensor is split into volumetric $\boldsymbol{\tau}^{\mathrm{v}}$ and deviatoric portions $\boldsymbol{\tau}^{\mathrm{d}}$:

$$\boldsymbol{\tau}^{\mathrm{v}} = P\mathbf{I} \tag{13}$$

$$\boldsymbol{\tau}^{\mathrm{d}} = \boldsymbol{\tau} - \boldsymbol{\tau}^{\mathrm{v}} \tag{14}$$

where $P = \frac{1}{3}(\tau_{11}+\tau_{22}+\tau_{33})$ is the pressure and $\mathbf{I}$ is the second-order identity tensor. Substituting (13) and (14) into (12) and collecting the deviatoric and volumetric portions yields

$$\underline{\hat{\mathbf{T}}}_{I:J} = \underline{\hat{\mathbf{T}}}^{\mathrm{d}}_{I:J} + \underline{\hat{\mathbf{T}}}^{\mathrm{v}}_{I:J}, \tag{15}$$

where

$$\underline{\hat{\mathbf{T}}}^{\mathrm{d}}_{I:J} = \omega_{I:J}\big(\boldsymbol{\tau}^{\mathrm{d}}_I\cdot\mathbf{F}_I^{-T}\cdot\mathbf{K}_I^{-1}\det(\mathbf{F}_I) + \boldsymbol{\tau}^{\mathrm{d}}_J\cdot{\mathbf{F}_J}^{-T}\cdot\mathbf{K}_J^{-1}\det(\mathbf{F}_J)\big)\cdot\mathbf{X}_{I:J} \tag{16}$$

and

$$\underline{\hat{\mathbf{T}}}^{\mathrm{v}}_{I:J} = \omega_{I:J}\big(P_I\mathbf{F}_I^{-T}\cdot\mathbf{K}_I^{-1}\det(\mathbf{F}_I) + P_J\mathbf{F}_J^{-T}\cdot\mathbf{K}_J^{-1}\det(\mathbf{F}_J)\big)\cdot\mathbf{X}_{I:J} \tag{17}$$

are the deviatoric and volumetric contributions, respectively. When applied to problem with strong shocks, the solution obtained by using these force states shows severe oscillations as the shock physics and Gibbs instability are not addressed. In this paper the essential shock physics is introduced into the volumetric force state by embedding Godunov scheme, which is to be discussed next.

In equation (17), on the right hand side, the first term involving P_I and the second term involving P_J physically represent the contribution to the volumetric force state between the two points I and J from each pressure of the points, or in other words they represent the force exchange between points

I and J due to pressure. In this paper, we introduce the Godunov scheme by solving the Riemann problem between point I and J to enrich this exchange. After solving the Riemann problem via Riemann solver, the Riemann solution enriched pressure and velocity are obtained $\{P^*_{IJ}, \mathbf{v}^*_I, \}$ ('*' denotes the Riemann solution), P^*_{IJ} is used to replace the P_J and P_J in equation (17), and in this manner, the entropy solution and jump conditions are embedded into the force state. Accordingly, $\underline{\hat{\mathbf{T}}}^{\mathrm{v}}_{I:J}$ becomes $\underline{\hat{\mathbf{T}}}^{\mathrm{v}*}_{I:J}$ and (17) becomes

$$\underline{\hat{\mathbf{T}}}^{\mathrm{v}*}_{I:J} = \omega_{I:J} P^*_{IJ} \big(\det(\mathbf{F}_I)\mathbf{F}_I^{-1} \cdot \mathbf{K}_I^{-1} + \det(\mathbf{F}_J)\mathbf{F}_J^{-1} \cdot \mathbf{K}_J^{-1}\big) \cdot \mathbf{X}_{I:J} \tag{18}$$

where P^*_{IJ} is the pressure solution of the Riemann problem between point I and J. The details about how to define and solve the Riemann problem is discussed in Section 3.2 and Section 4.2.

Finally, the equation of motion after embedding Godunov scheme is

$$\rho_I \ddot{\mathbf{u}}_I - \int_{\mathrm{H}_{\mathbf{x}_I}} \big[\underline{\hat{\mathbf{T}}}^{\mathrm{d}}_{I:J}\langle \mathbf{X}_{I:J}\rangle + \underline{\hat{\mathbf{T}}}^{\mathrm{v}*}_{I:J}\langle \mathbf{X}_{I:J}\rangle\big] dV_{\mathbf{X}_J} - \mathbf{b}_I = 0 \tag{19}$$

where $\underline{\hat{\mathbf{T}}}^{\mathrm{d}}_{I:J}$ and $\underline{\hat{\mathbf{T}}}^{\mathrm{v}*}_{I:J}$ are given in (16) and (18). The resulting formulation is termed Godunov-peridynamics.

3.2 Discussion

To examine the properties of the algorithm and to define the Riemann problem, (18) is first rewritten in the following form

$$\underline{\hat{\mathbf{T}}}^{\mathrm{v}*}_{I:J} = P^*_{IJ}\boldsymbol{\alpha}_{IJ} \tag{20}$$

with

$$\boldsymbol{\alpha}_{IJ} = \mathbf{F}_I^{-T} \cdot \mathbf{K}_I^{-1} \cdot \mathbf{X}_{I:J}\det(\mathbf{F}_I)\omega_{I:J}, + \mathbf{F}_J^{-T} \cdot \mathbf{K}_J^{-1} \cdot \mathbf{X}_{I:J}\det(\mathbf{F}_J)\omega_{I:J}. \tag{21}$$

With nodal integration (further discussed in Section 4.1), the driving internal force density $\mathbf{f}_I^{\mathrm{v}*}$ at point I due to pressure in (20) is expressed as

$$\mathbf{f}_I^{\mathrm{v}*} = \sum_{J\in\mathcal{N}_I} P^*_{IJ}\boldsymbol{\alpha}_{IJ} V_J \tag{22}$$

where $\mathcal{N}_I$ is the set containing the point indices within the horizon of point I and V_J is the integration weight assigned to point J. The term $\boldsymbol{\alpha}_{IJ}$ in the above can be seen to control the contribution of the pressure to a given point I from point J.

On the other hand, a finite volume method calculates the driving force $\bar{\mathbf{f}}_I^{\mathrm{v}*}$ from the enriched pressure for a cell I from faces J of its neighboring cells as [31]

$$\bar{\mathbf{f}}_I^{\mathrm{v}*} = \sum_{J\in\mathcal{F}_I} P^*_{IJ}\bar{\boldsymbol{\alpha}}_{IJ} V_J \tag{23}$$

where $\mathcal{F}_I$ is the set containing faces indices for cell I, and

$$\bar{\boldsymbol{\alpha}}_{IJ} = \frac{\boldsymbol{n}_{IJ} A_{IJ}}{V_I V_J} \tag{24}$$

is the equivalent coefficient for the finite volume method, with $\boldsymbol{n}_{IJ}$ the surface normal and A_{IJ} the surface area shared by cell I and J. Therefore the coefficient $\boldsymbol{\alpha}_{IJ}$ for the proposed formulation can be interpreted as containing effective surface information between point pairs, with $\mathbf{n}^\alpha = \boldsymbol{\alpha}_{IJ}/|\boldsymbol{\alpha}_{IJ}|$ the effective normal, and will be the basis of the present Godonuv implementation in Section 4.2.

Note that by substituting $\mathbf{X}_{I:J} = -\mathbf{X}_{I:J}$ into (21), it is obvious that

$$\boldsymbol{\alpha}_{IJ} = -\boldsymbol{\alpha}_{JI}. \tag{25}$$

This anti-symmetric property is again shared by finite volume cells where the normal of one cell is opposite to that shared by its neighboring cells yielding $\bar{\boldsymbol{\alpha}}_{IJ} = -\bar{\boldsymbol{\alpha}}_{JI}$, which is critical to ensure conservation in finite volume method [31]. The anti-symmetric property of $\boldsymbol{\alpha}_{IJ}$ in the present formulation means that the force exchange due to pressure between point I and J are equal and opposite in the case that $V_I = V_J$.

4 Numerical implementation

This section describes the numerical implementation of Godunov-peridynamics. Nodal quadrature used to numerically evaluate domain integrals is given, along with the Riemann problem solution and time integration procedures.

4.1 Nodal integration

As can be seen, $\mathbf{F}$ in (3), $\mathbf{K}$ in (4), and the second term in (19) require numerical integration. After discretization as shown in Figure 1, the nodal integration scheme is employed [32] and these terms are computed as

$$\mathbf{K}_I = \sum_{J \in \mathcal{N}_I} \omega_{I:J} \mathbf{X}_{I:J} \otimes \mathbf{X}_{I:J} V_J, \tag{26}$$

$$\mathbf{F}_I = \sum_{J \in \mathcal{N}_I} \omega_{I:J} \mathbf{x}_{I:J} \otimes \mathbf{X}_{I:J} V_J, \tag{27}$$

and

$$\rho_I \ddot{\mathbf{u}}_I - \sum_{J \in \mathcal{N}_I} \left[\hat{\underline{\mathbf{T}}}^{\mathrm{d}}_{I:J} \langle \mathbf{X}_{I:J} \rangle + \hat{\underline{\mathbf{T}}}^{\mathrm{v}*}_{I:J} \langle \mathbf{X}_{I:J} \rangle \right] V_J - \mathbf{b}_I = 0. \tag{28}$$

While the quadrature employed is inherently low-order, influence functions such as the cubic spline (5) help to reduce inaccuracy in integration and yield more consistent solution convergence behavior [30].

4.2 Riemann solution

In (18), the term $\hat{\underline{\mathbf{T}}}^{\mathrm{v}*}_{I:J}$ involves P^*_{IJ} which is obtained by solving the Riemann problem at the middle point between point I and J.

First, a piece-wise distribution in pressure and velocity is assumed to eliminate Gibbs instability: between point I and the middle point, and point J and the middle point, the pressure and velocity is assumed to be constant. The Riemann problem is then solved along the effective normal direction between the two nodes in the deformed configuration $\mathbf{n}^\alpha = \boldsymbol{\alpha}_{IJ}/|\boldsymbol{\alpha}_{IJ}|$, as shown in Figure 2, with the normal velocity calculated as

$$v_I^{\alpha-\mathrm{n}} = \mathbf{v}_I \cdot \mathbf{n}^\alpha. \tag{29}$$

The Riemann problem then consists of a left state $\{P_I, v_I^{\alpha-\mathrm{n}}, \rho_I\}$ and right state $\{P_J, v_J^{\alpha-\mathrm{n}}, \rho_J\}$, with the solution $\{P^*_{IJ}, v^{\alpha-\mathrm{n}*}_{IJ}\}$. In the Appendix, the Dukowicz Riemann solver [33] employed in this work is given for convenience.

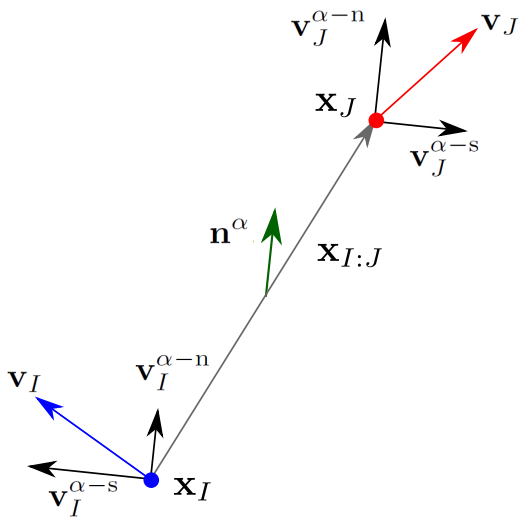

Figure 2: Velocity projection in the deformed configuration.

4.3 Time integration procedures

For clarity in describing the time integration procedure, equation (28) is rewritten in the following form,

$$\rho_I \ddot{\mathbf{u}}_I = \mathbf{f}_I^{\mathrm{d}} + \mathbf{f}_I^{\mathrm{v}^*} + \mathbf{b}_I, \tag{30}$$

with

$$\mathbf{f}_I^{\mathrm{d}} = \sum_{J \in \mathcal{N}_I} \left[\hat{\underline{\mathbf{T}}}_{I:J}^{\mathrm{d}} \langle \mathbf{X}_{I:J} \rangle\right] V_J, \tag{31}$$

$$\mathbf{f}_I^{\mathrm{v}^*} = \sum_{J \in \mathcal{N}_I} \left[\hat{\underline{\mathbf{T}}}_{I:J}^{\mathrm{v}^*} \langle \mathbf{X}_{I:J} \rangle\right] V_J. \tag{32}$$

The Newmark-beta method is employed to perform temporal discretization of equation (30) with $\beta = 0$, and $\gamma = \frac{1}{2}$ resulting in the explicit central difference scheme. In what follows, the superscript (n) denotes a variable at the n^{th} time step. The central difference time integration procedures for a point I in a predictor-corrector implementation are given as:

(1) Initialization:

   (a) Form initial $\mathbf{b}_I^{(0)}$.

   (b) Calculate initial acceleration $\mathbf{a}_I^{(0)}$ by
   $\rho_I \mathbf{a}_I^{(0)} = \mathbf{b}_I^{(0)}$.

(2) At the $(n+1)^{th}$ time step:

   (a) Predictor phase: calculate displacement predictor $\tilde{\mathbf{u}}_I$ and velocity predictor $\tilde{\mathbf{v}}_I$
   $\tilde{\mathbf{u}}_I^{(n+1)} = \mathbf{u}_I^{(n)} + \Delta t \mathbf{v}_I^{(n)} + \frac{\Delta t^2}{2} \mathbf{a}_I^{(n)}$,
   $\tilde{\mathbf{v}}_I^{(n+1)} = \mathbf{v}_I^{(n)} + \frac{\Delta t}{2} \mathbf{a}_I^{(n)}$.

   (b) Calculate $\boldsymbol{\tau}_I^{\mathrm{d}(n+1)}$ and $P_I^{(n+1)}$.

   (c) Calculate Riemann solution for point I's pairs.

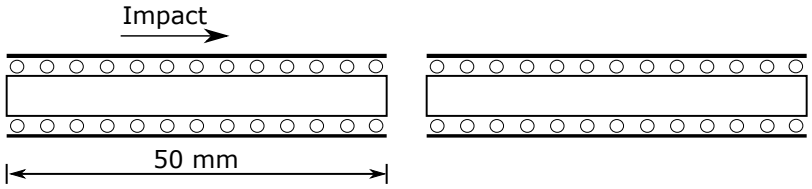

Figure 3: Schematic of one-dimensional elastic bar impact problem.

(d) Calculate $\mathbf{f}_I^{\mathrm{d}(n+1)}$ and $\mathbf{f}_I^{\mathrm{v}^*(n+1)}$ according to equation (31) and (32) respectively, and also compute $\mathbf{b}_I^{(n+1)}$.

(e) Solve $\rho_I \mathbf{a}_I^{(n+1)} = \mathbf{f}_I^{\mathrm{d}(n+1)} + \mathbf{f}_I^{\mathrm{v}^*(n+1)} + \mathbf{b}_I^{(n+1)}$ for acceleration $\mathbf{a}_I^{(n+1)}$.

(f) Corrector phase:
$\mathbf{v}_I^{(n+1)} = \mathbf{v}_I^{(n)} + \frac{\Delta t}{2}(\mathbf{a}_I^{(n)} + \mathbf{a}_I^{(n+1)})$,
$\mathbf{u}_I^{(n+1)} = \tilde{\mathbf{u}}_I^{(n+1)}$.

(3) If time t is less than the total simulation time t_{final}, set $n \to n+1$ and go to (a) in step (2).

5 Numerical Examples

In all the numerical examples, uniform point distributions are used; the radius of the horizon is set to be 1.65 times the spacing; and the cubic spline influence function (5) is employed. All examples are impact problems. The impact is not explicitly modeled as a contact condition, instead it is achieved by modeling the impact and target objects as one body with different initial velocities, where the shock physics moments before the bars physically separate are observed. The terms 'peridynamics' and 'Godunov-peridynamics' are used to denote the results obtained by the non-ordinary state-based peridynamics and the proposed Godunov-peridynamics formulations.

5.1 Elastic bar impact

A one-dimensional elastic bar impact problem shown in Figure 3 is solved as the first example. The bars are made of 6061 T-6 aluminum, which is described by a J_2 perfect plasticity material model. The material properties are given as Young's modulus $E = 77.11$ GPa, Poisson's ratio $\nu = 0.334$, density $\rho = 2703$ kg/m^3, and yield strength $Y_0 = 270$ MPa. The deformation is only allowed along the axial direction and the lateral direction is constrained by rollers (see Figure 3). The initial velocity of the impact bar is 3.00×10^4 mm/sec, and that of the target bar is 0.00 mm/sec, which results in elastic waves in the bars due to the relatively low impact velocity. Both bars have a length of 50 mm, and are discretized with 800 points in the axial direction. The analytical solution of this problem can be derived by making use of the Rankine-Hugoniot jump conditions (see [34]). We consider the solution at two different moments: at time 6 µsec (before free end reflection) and time 10 µsec (after free end reflection).

The numerical solutions by peridynamics and Godunov-peridynamics at time 6 µsec are given in Figure 4. After free end reflection, at time 10 µsec, the resulting axial stress and velocity magnitudes remain the same as at time 6 µsec. The associated numerical results for both formulations are shown in Figure 5. As can be seen, the results by peridynamics in both cases show severe oscillations in stresses and velocity.

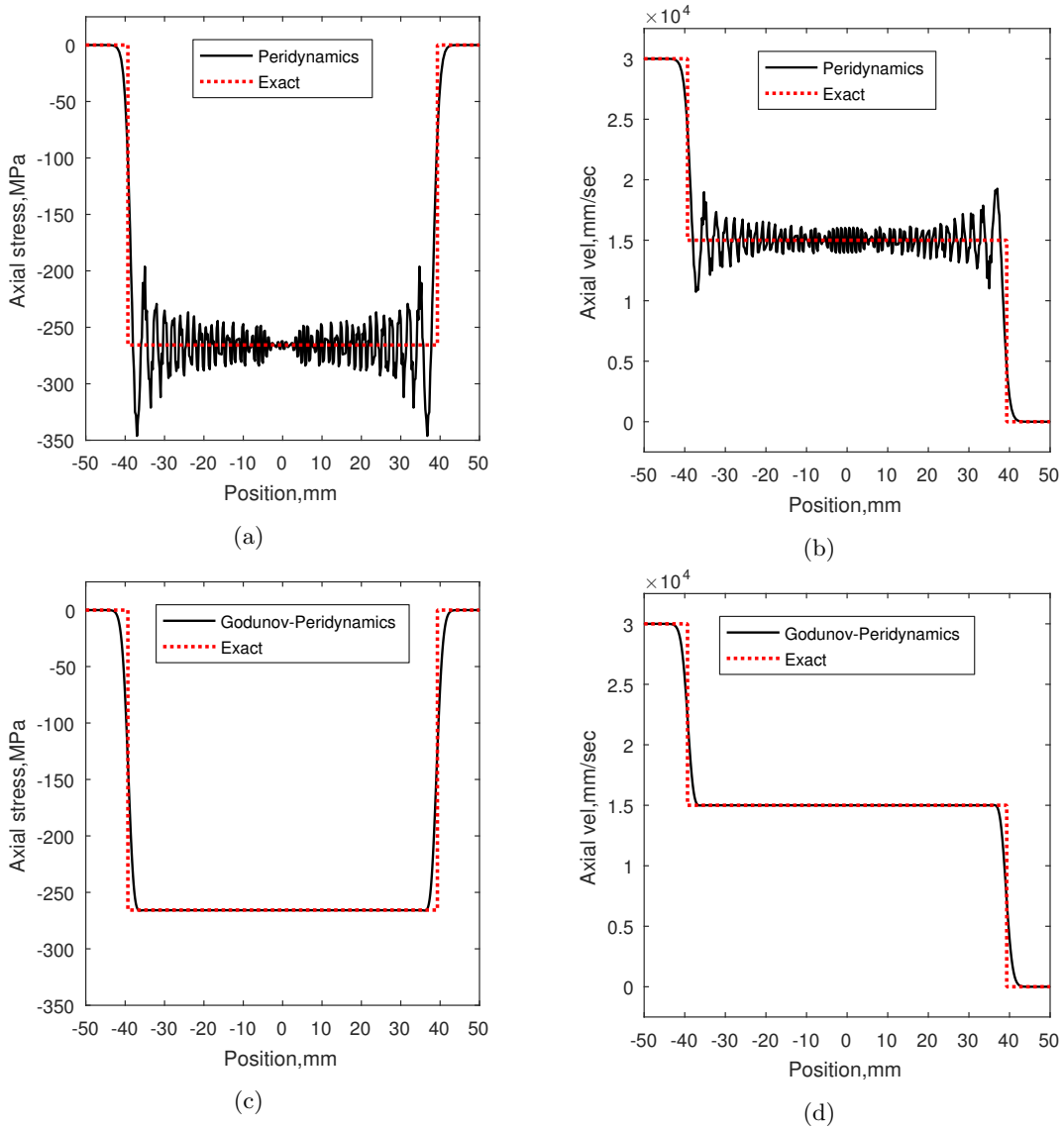

Figure 4: One-dimensional elastic bar impact: axial stress and velocity distribution at time $t = 6$ µsec, (a) and (b) by peridynamics, (c) and (d) by Godunov-peridynamics.

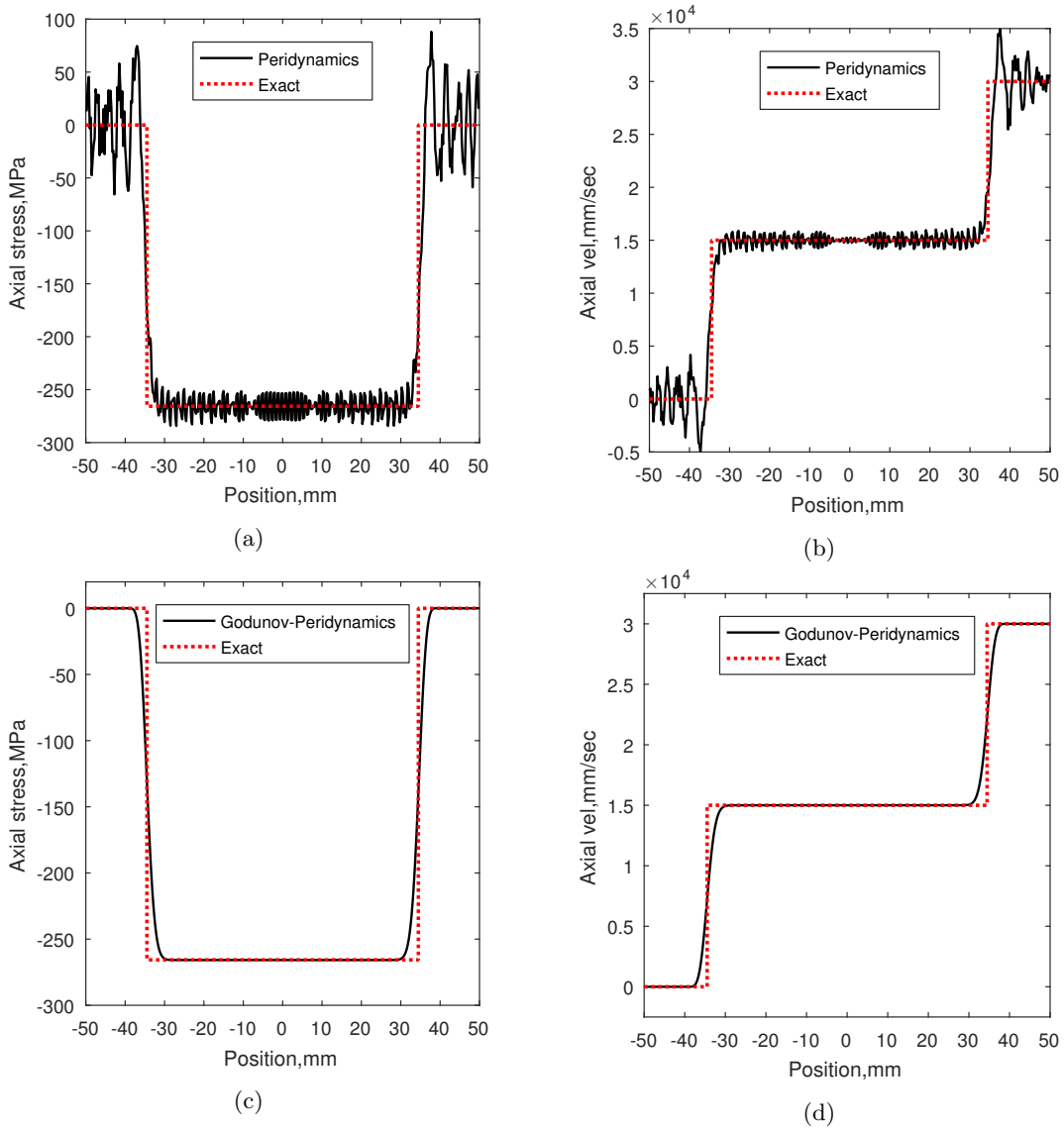

Figure 5: Elastic bar impact: axial stress and velocity distribution at time $t = 10$ µsec, (a) and (b) by peridynamics, (c) and (d) by Godunov-peridynamics.

5.2 Elasto-plastic bar impact

This problem is similar to the example in section 5.1 but with a higher impact velocity 2.73 $\times 10^5$ mm/sec. The geometry size, material properties, boundary conditions, and discretization of the bars are the same as in the previous problem. The higher impact velocity of 2.73 $\times 10^5$ mm/sec is chosen such that the yield strength is reached, and as a result, an elastic shock wave is formed, followed by a plastic shock wave. Here the solution at time 6 µsec is examined. The numerical solutions by peridynamics and Godunov-peridynamics are given in Figure 6 and compared with the exact solution [34]. Both formulations give the correct shock speeds and jump magnitudes if the averaged magnitudes are used for the oscillatory peridynamics results, however, the peridynamics solutions show severe oscillation, while Godunov-peridynamics formulation offers a non-oscillatory solution. A set of discretizations, 400 points, 800 points, and 1600 points in the axial direction are used to check the solution convergence, and the result is given in Figure 7. In the enlarged subfigure, one can observe that the numerical solution by Godunov-peridynamics converges.

5.3 High velocity plate impact

Here, a two-dimensional plane-strain high velocity plate impact problem is modeled. A flyer plate with a velocity of 1.00 $\times 10^6$ mm/sec impacts another plate that is initially static. All in-plane edges are unconstrained resulting in multi-dimensional wave propagation. After the compression shock wave reaches the free surface, a rarefaction wave is formed and propagates inside from the outer edges. Each plate is 8 mm wide by 2 mm thick (see Figure 8), and are discretized as 161 points by 41 points, in each direction respectively. The impact occurs along the longer 8 mm edge. The material is again 6061 T-6 aluminum, modeled with the same material properties and constitutive model as in the previous problems. The pressure contours at time $t = 0.075$ µsec and $t = 0.25$ µsec are provided in Figure 9. Consistent with the above discussion, a compression shock wave is first generated and then propagates along the impact direction, and a rarefaction wave forms from the lateral edges, which relieves the pressure in the initially compression-loaded zone. Peak pressure behind the shock wave was experimentally measured by Marsh [35] as 8.00 GPa. Here the result by peridynamics is 9.01 GPa with 12.63% error whereas Godunov-peridynamics gives a more accurate peak pressure of 7.61 GPa with 4.87 % error. On the other hand, the two pressure contours by Godunov-peridynamics at two these time instances are both essentially free of oscillation while the solutions by peridynamics are highly oscillatory. This example also shows the ability to accurately solve problems involving multi-dimensional shockwave propagation by Godunov-peridynamics.

6 Conclusion

In this paper, a shock modeling formulation termed Godunov-peridynamics is proposed that incorporates shock physics by employing the Godunov scheme into non-ordinary state-based peridynamics. The essential shock physics of entropy and jump conditions are considered by introducing the Riemann problem solution into the volumetric portion of the force state. The Riemann problem is defined at the middle point of each point pair via effective surface information $\boldsymbol{\alpha}$ in the deformed configuration. The anti-symmetric property of $\boldsymbol{\alpha}$ ensures a volumetric force state conservation in uniform discretizations where equal integration weights are employed. The resulting formulation does not introduce any tunable parameters and controls the oscillations otherwise induced by shocks.

This work also provides a general technique to bridge the Godunov scheme and other numerical methods when effective surface information $\boldsymbol{\alpha}$ in (22) can be obtained.

Several benchmark problems involving one-dimensional and two-dimensional shocks are examined, where non-oscillatory solutions with high accuracy are obtained under the present formulation. Future effort will be devoted to applying this formulation to shock-induced fragmentation by incorporating bond-breakage and material damage.

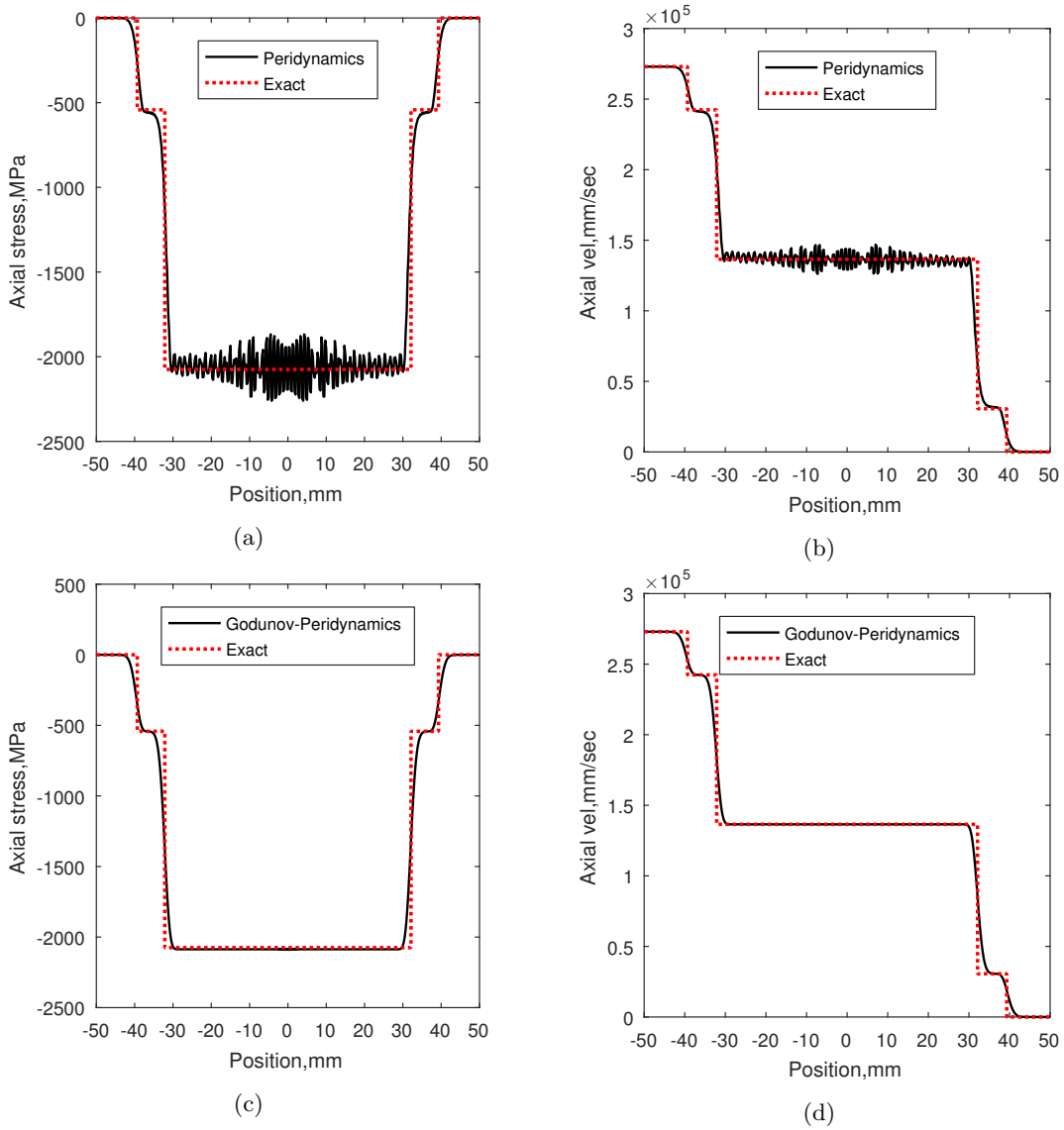

Figure 6: Elasto-plastic bar impact: axial stress and velocity distribution at time $t = 6$ µsec, (a) and (b) by peridynamics, (c) and (d) by Godunov-peridynamics.

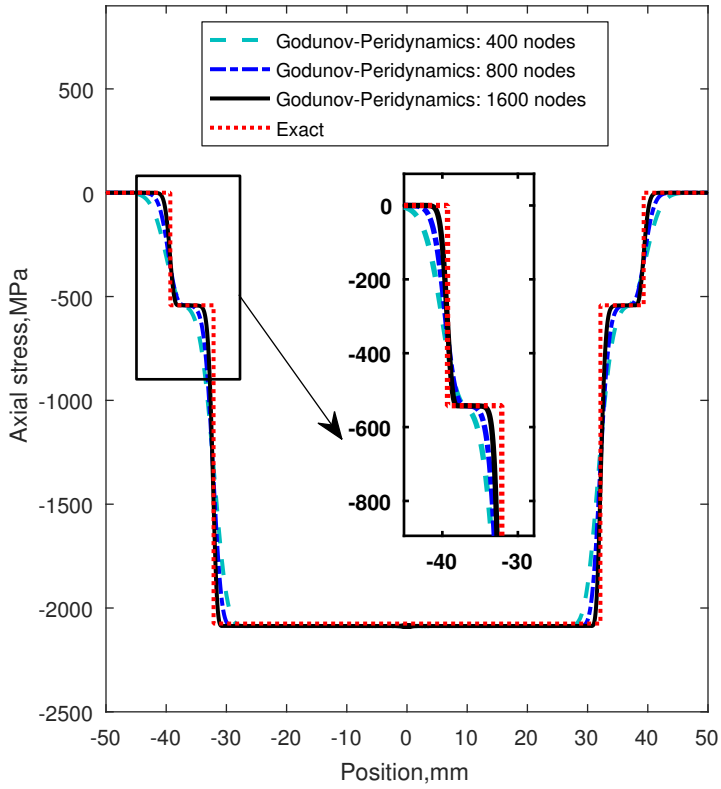

Figure 7: One-dimensional elasto-plastic bar impact: axial stress distribution with different discretizations at time $t = 6$ µsec.

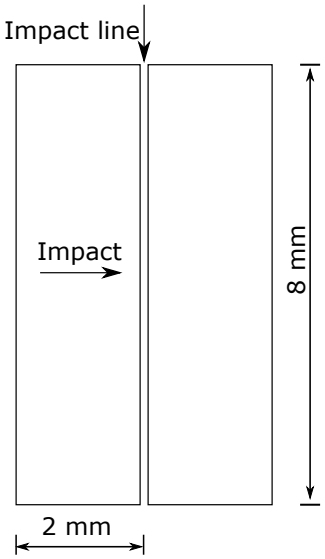

Figure 8: Schematic of high velocity plate impact problem.

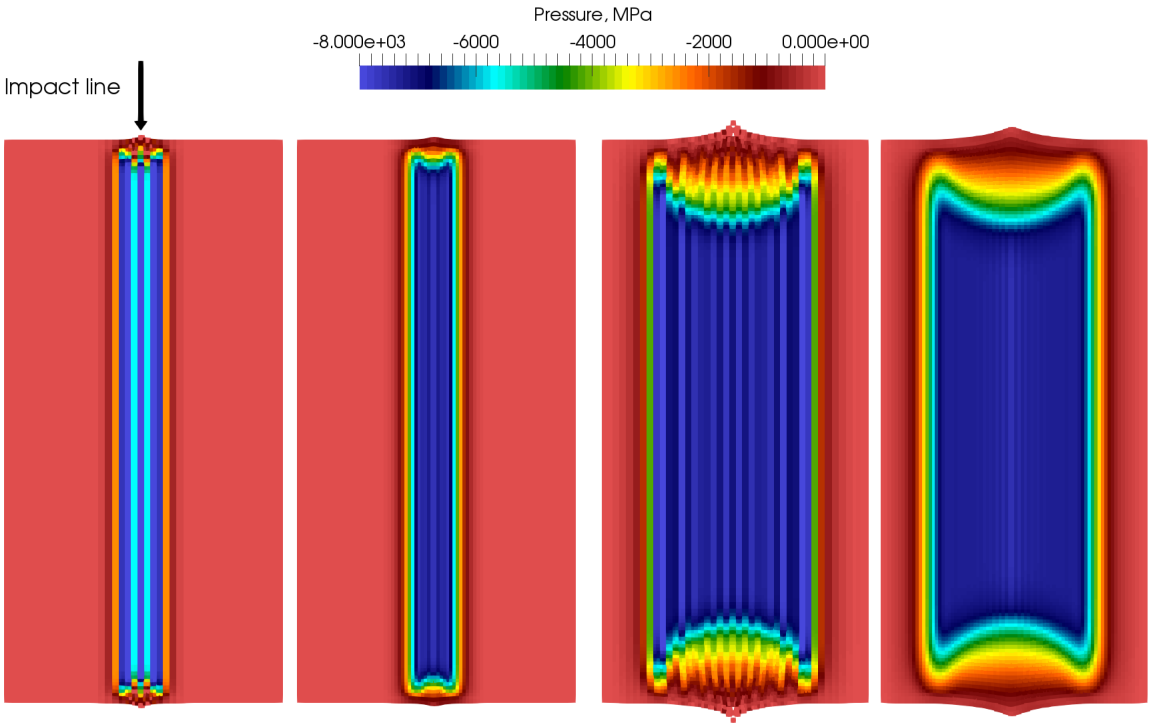

Figure 9: High velocity plate impact pressure contours: left two (left to right), peridynamics and Godunov-peridynamics results at time $t = 0.075$ µsec, and right two (left to right), peridynamics and Godunov-peridynamics results at time $t = 0.25$ µsec.

Acknowledgments The authors greatly acknowledge the support of this work by the College of Engineering at Penn State.

Conflict of interest statement

On behalf of all authors, the corresponding author states that there is no conflict of interest.

Appendix

Here an brief overview of the Dukowicz Riemann solver [33] employed in this work is given. Consider a left state $\{P_L, \mathrm{v}_L, \rho_L\}$ and right state $\{P_R, \mathrm{v}_R, \rho_R\}$, with the solution $\{P^*, \mathrm{v}^*\}$. In this solver, the velocity v* is first computed by solving the following semi-quadratic equation,

$$\rho_L B_L \big|\mathrm{v}^* - \mathrm{v}^*_{min}\big|\big(\mathrm{v}^* - \mathrm{v}^*_{min}\big) + \rho_R B_R \big|\mathrm{v}^* - \mathrm{v}^*_{max}\big|\big(\mathrm{v}^* - \mathrm{v}^*_{max}\big) + P^*_L - P^*_R, \tag{33}$$

where

$$\begin{aligned} \mathrm{v}^*_{min} = \mathrm{v}_L - 0.5C_L/B_L, \qquad \mathrm{v}^*_{max} = \mathrm{v}_R - 0.5C_R/B_R; \\ P^*_L = P_L - 0.25\rho_L\big(C_L\big)^2/B_L, \qquad P^*_R = P_R - 0.25\rho_R\big(C_R\big)^2/B_R. \end{aligned} \tag{34}$$

Here C is the speed of sound, and B is a parameter that is directly related to the shock density ratio in the limit of strong shocks (for more details, refer to [33]). Equation (33) becomes a quadratic equation after assuming a sign for $\big(\mathrm{v}^* - \mathrm{v}^*_{min}\big)$ and $\big(\mathrm{v}^* - \mathrm{v}^*_{max}\big)$ yielding four cases in total. One of the two roots of each quadratic equation can be abandoned in advance and the other root left is the unique solution for each case. Once the velocity v* is solved, the pressure solution P^* can be readily calculated by the following equation,

$$P^* = 0.5\big(P^*_L + P^*_R\big) + 0.5\rho_L B_L \big|\mathrm{v}^* - \mathrm{v}^*_{min}\big|\big(\mathrm{v}^* - \mathrm{v}^*_{max}\big) - 0.5\rho_R B_R \big|\mathrm{v}^* - \mathrm{v}^*_{max}\big|\big(\mathrm{v}^* - \mathrm{v}^*_{min}\big). \tag{35}$$

As can be seen, this Riemann solver is non-iterative.

In the end, the obtained P^* is used as P^*_{IJ} in (18) to compute the Riemann solution enriched volumetric force state.

References

[1] S.A. Silling. Reformulation of elasticity theory for discontinuities and long-range forces. *Journal of the Mechanics and Physics of Solids*, 48(1):175–209, 2000.

[2] S.A. Silling, M. Epton, O. Weckner, J. Xu, and E. Askari. Peridynamic states and constitutive modeling. *Journal of Elasticity*, 88(2):151–184, 2007.

[3] Y.D. Ha and F. Bobaru. Studies of dynamic crack propagation and crack branching with peridynamics. *International Journal of Fracture*, 162(1-2):229–244, 2010.

[4] F. Bobaru and G. Zhang. Why do cracks branch? a peridynamic investigation of dynamic brittle fracture. *International Journal of Fracture*, 196(1-2):59–98, 2015.

[5] F. Bobaru, Y.D. Ha, and W. Hu. Damage progression from impact in layered glass modeled with peridynamics. *Central European Journal of Engineering*, 2(4):551–561, 2012.

[6] W. Gerstle, N. Sau, and S. Silling. Peridynamic modeling of concrete structures. *Nuclear Engineering and Design*, 237(12-13):1250–1258, 2007.

[7] M.R. Tupek, J.J. Rimoli, and R. Radovitzky. An approach for incorporating classical continuum damage models in state-based peridynamics. *Computer Methods in Applied Mechanics and Engineering*, 263:20–26, 2013.

[8] J.T. Foster, S.A. Silling, and W.W. Chen. Viscoplasticity using peridynamics. *International Journal for Numerical Methods in Engineering*, 81(10):1242–1258, 2010.

[9] T.L. Warren, S.A. Silling, A. Askari, O. Weckner, M.A. Epton, and J. Xu. A non-ordinary state-based peridynamic method to model solid material deformation and fracture. *International Journal of Solids and Structures*, 46(5):1186–1195, 2009.

[10] B. Ren, H. Fan, G.L. Bergel, R.A. Regueiro, X. Lai, and S. Li. A peridynamics-SPH coupling approach to simulate soil fragmentation induced by shock waves. *Computational Mechanics*, 55(2):287–302, 2014.

[11] X. Lai, L. Liu, S. Li, M. Zeleke, Q. Liu, and Z. Wang. A non-ordinary state-based peridynamics modeling of fractures in quasi-brittle materials. *International Journal of Impact Engineering*, 111:130–146, 2018.

[12] S.A. Silling, M.L. Parks, J.R. Kamm, O. Weckner, and M. Rassaian. Modeling shockwaves and impact phenomena with eulerian peridynamics. *International Journal of Impact Engineering*, 107:47–57, 2017.

[13] S.K. Godunov. A finite difference method for numerical computation of discontinuous solutions of the equations of fluid dynamics. *Sbornik: Mathematics, translated US Joint Publications Research Service, JPRS*, 47:271–306, 1969.

[14] B. Cockburn and C.W. Shu. The Runge-Kutta discontinuous galerkin method for conservation laws V. *Journal of Computational Physics*, 141(2):199–224, 1998.

[15] S.I. Inutsuka. Reformulation of smoothed particle hydrodynamics with Riemann solver. *Journal of Computational Physics*, 179(1):238–267, 2002.

[16] R. Löhner, C. Sacco, E. Oñate, and S.R. Idelsohn. A finite point method for compressible flow. *International Journal for Numerical Methods in Engineering*, 53(8):1765–1779, 2002.

[17] J.K. Dukowicz, M.C. Cline, and F.L. Addessio. A general topology Godunov method. *Journal of Computational Physics*, 82(1):29–63, 1989.

[18] D. Hietel, K. Steiner, and J. Struckmeier. A finite volume particle method for compressible flows. *Mathematical Models and Methods in Applied Science*, 10:1363–1382, 2000.

[19] E.K. Chiu, Q. Wang, and A. Jameson. A conservative meshless scheme: general order formulation and application to euler equations. In *AIAA 2011-651 49th Aerospace Sciences Meeting*, 2011.

[20] H. Luo, J.D. Baum, and R. Loehner. Edge-based finite element scheme for the euler equations. *AIAA journal*, 32(6), 1994.

[21] C. Praveen. A positive meshless method for hyperbolic equations. Technical report, 2004.

[22] Z.H. Ma, H. Wang, and L. Qian. A meshless method for compressible flows with the HLLC Riemann solver. *arXiv preprint arXiv:1402.2690*, 44(0):1–24, 2014.

[23] X.D. Liu, S. Osher, and T. Chan. Weighted essentially non-oscillatory schemes. *Journal of Computational Physics*, 115(1):200–212, 1994.

[24] B. van Leer. Towards the ultimate conservative difference scheme. V. A second-order sequel to Godunov's method. *Journal of Computational Physics*, 32(1):101–136, 1979.

[25] W.K. Liu, S. Jun, and Y.F. Zhang. Reproducing kernel particle methods. *International Journal for Numerical Methods in Fluids*, 20(8-9):1081–1106, 1995.

[26] J.S. Chen, C. Pan, C.T. Wu, and W.K. Liu. Reproducing kernel particle methods for large deformation analysis of non-linear structures. *Computer Methods in Applied Mechanics and Engineering*, 139(1-4):195–227, 1996.

[27] J.S. Chen, C.T. Wu, S. Yoon, and Y. You. A stabilized conforming nodal integration for galerkin mesh-free methods. *International Journal for Numerical Methods in Engineering*, 50(2):435–466, 2001.

[28] M.J. Roth, J.S. Chen, K.T. Danielson, and T.R. Slawson. Hydrodynamic meshfree method for high-Rate solid dynamics using a Rankine-Hugoniot enhancement in a Riemann-SCNI framework. *International Journal for Numerical Methods in Engineering*, 2016.

[29] M.J. Roth, J.S. Chen, T.R. Slawson, and K.T. Danielson. Stable and flux-conserved meshfree formulation to model shocks. *Computational Mechanics*, 57(5):773–792, 2016.

[30] P. Seleson and D.J. Littlewood. Convergence studies in meshfree peridynamic simulations. *Computers and Mathematics with Applications*, 71(11):2432–2448, 2016.

[31] R.J. LeVeque. *Finite volume methods for hyperbolic problems*, volume 31. Cambridge University Press, 2002.

[32] S.A. Silling and E. Askari. A meshfree method based on the peridynamic model of solid mechanics. *Computers and Structures*, 83(17-18):1526–1535, 2005.

[33] J.K. Dukowicz. A general, non-iterative Riemann solver for Godunov's method. *Journal of Computational Physics*, 61(1):119–137, 1985.

[34] L. Davison. Fundamentals of shock wave propagation in solids. Springer-Verlag, Berlin, 2008.

[35] S.A. Marsh. LASL shock hugoniot data. Technical report, University of California Press, Berkley, 1980.